

STUDY ON THE SPATIAL GENERATION OF BREAKDOWN SPOTS IN MIM CAPACITORS WITH DIFFERENT ASPECT RATIOS

Xavier Saura¹, Michele Riccio², Giuseppe De Falco², Jordi Suñé¹,
Andrea Irace², Enrique Miranda¹

¹Departament d'Enginyeria Electrònica,

Universitat Autònoma de Barcelona, Barcelona, Spain

²Department of Electrical Engineering and Information Technologies,
University of Naples Federico II, Naples, Italy

Abstract. *Metal-insulator-metal (MIM) large area ($>10^4$ cm²) capacitors with different aspect ratios were subjected to severe stress conditions ($E_{ox}>4-5$ MV/cm) with the aim of generating a large density of breakdown spots (from 10^5 to 10^6 spots/cm²) in the same device. The resulting mark pattern on the top metal electrode associated with the failure events was analyzed first using conventional functional estimators for two-dimensional spatial statistics. Second, as a double check, the attention was focused on the same breakdown spot patterns but in relation to the probe point location. In this latter case, the objective was to rule out any stochastic dependence of the breakdown spot distribution on the position of the source of degradation and therefore to confirm whether or not the spots follow a complete spatial randomness (CSR) process. In order to simplify the mathematical treatment of the point-to-event distributions, the voltage probe was assumed to be located at one corner of the observation window which significantly reduces the number of cases to analyze. Infrared images revealed that the generation of the spots is associated with micro-explosions within the insulating material (HfO₂) and with the local volatilization of the top metal electrode (Pt).*

Key words: *oxide breakdown, oxide reliability, infrared thermography, HfO₂*

1. INTRODUCTION

Failure analysis of thin dielectric films in metal-insulator-metal (MIM) and metal-insulator-semiconductor (MIS) devices consists in the application of controlled electrical stress and the determination of lifetime estimates using accelerated degradation tests [1,2]. In order to achieve good estimates a large number of devices need to be subjected to identical stressing conditions until a failure event is detected according to a pre-established criterion (current or voltage jump, progressive leakage current increase, anomalous noise

Received January 5, 2015

Corresponding author: Enrique Miranda

Departament d'Enginyeria Electrònica, Universitat Autònoma de Barcelona, 08193 Cerdanyola del Vallés,
Barcelona, Spain

(e-mail: Enrique.Miranda@uab.cat)

increment in the measurements, etc.). In this way, the time-to-breakdown (BD) statistics using multiple units is constructed. However, the fact that each device provides a single data point to the sampling distributions is a limiting factor for data collection and a time-consuming process which in general requires careful planning and execution. Fortunately, it has been demonstrated that in certain cases more than one failure event per device can be generated and detected by means of electrical methods, mainly using constant voltage stress (CVS) tests. The successive BD statistics has been used not only to estimate the lifetime of devices but also the temporal and spatial correlations among the failure events [3]. In [4], the successive failure event statistics was obtained assuming Poisson area scaling for large virtual area devices and the weakest link property of dielectric BD. Although this procedure allows examining large data sets (with a single BD event per device) and assessing their order statistics, the method cannot be considered a direct proof of uncorrelated events. On the other hand, in this work, the attention is particularly focused on the spatial correlation of multiple failure events occurring in the same device. The temporal correlation of the BD events was investigated in [5] and it was shown to be consistent with a homogeneous Poisson process.

From the microscopic viewpoint, it is well known that during electrical stress, defects or traps are generated within the dielectric film which ultimately leads to the creation of a filamentary pathway spanning the oxide layer [6]. The formation of this path and the consequent leakage current increase is identified as a BD event. If the occurrence of this event is sufficiently energetic, the damage becomes visible on the top electrode as a mark associated with the local volatilization of the metal layer. Since during the application of CVS the degradation of the device does not stop after the occurrence of the first BD event, it is possible therefore to generate more than a single mark per device. At the outset, the BD spot generation rate is governed by the magnitude of the stress voltage but as the degradation proceeds, it becomes limited by the interplay of the current that flows through the parallel BD paths and the voltage drop across the series resistance associated with the device itself or with the measurement setup. When the oxide voltage reduces, the generation of spots ends. The final result is a visible point pattern on the top electrode material that can be analyzed using the methods of two-dimensional (2-D) spatial statistics [7,8]. Functional estimators and point-to-event distributions are used then to assess the statistical properties of these failure events. In addition, in order to illustrate the origin of the BD spot pattern, we used the transient infrared (IR) thermography characterization technique, which is based on a real-time mapping of the thermal activity of the device during the degradation stage. Interestingly, the methods described here are particularly relevant for devices exhibiting the resistive switching (RS) effect, which basically consists in the formation and rupture of a single or multiple conduction channels spanning the dielectric layer in a MIM structure [9]. In this regard, several papers have reported the appearance of degradation patterns on the top metal electrode of the structures during the switching process arising from the out-diffusion of oxygen ions from the oxide layer [9,10]. Although this subject is out of the scope of this paper, it is worth mentioning that multifilamentary RS is currently being considered for multilevel memory devices and could represent a breakthrough in the field of large capacity information storage systems [11].

This paper is organized as follows: in Section II, the samples under investigation and the experimental setup used to characterize the IR emission during the multiple dielectric breakdown process are described. In Section III, the generation of the BD spot pattern and the associated thermal effects are discussed. In Section IV, the spatial distribution of

the failure events is investigated using conventional functional estimators for 2-D spatial point processes. In all the cases, the estimated curves are accompanied by the corresponding 95% confidence bands. In Section V, the same BD spot patterns are examined using distance and angular point-to-event probability distributions for rectangular area observation windows. In this case, the probe point location is considered as the reference point from which the distances and angles to the BD events are computed. For the sake of mathematical simplicity, the point probe is considered to be located at one of the vertices of the observation window. Finally, in Section VI, the conclusions of this work are presented.

2. SAMPLES AND EXPERIMENTAL SETUP

The devices investigated were MIM capacitors fabricated according to the following steps: a 200 nm-thick thermal SiO₂ layer was grown on a n-type Si (100) substrate, after which a Pt (200 nm-thick) layer was deposited by electron-beam (E-beam) evaporation. The samples were then placed in a Cambridge NanoTech Fiji atomic layer deposition (ALD) system where HfO₂ (30 nm-thick) was deposited using TEMA₂Hf precursor and H₂O. The samples were then returned to the E-beam evaporator and a Pt layer (200 nm-thick) was deposited on top of the HfO₂ film. Lithography and a lift-off process were used to form arrays of rectangular capacitors of different sizes (400 x 400 μm², 400 x 100 μm², 1600 x 100 μm²). Access to the bottom Pt metal was enabled via a dry etching technique using a mask/resist process that removed the HfO₂ to the bottom Pt metal while at the same time protected the top Pt metal of the patterned devices. The oxide extends 25 μm beyond the perimeter edge of the top metal electrode. The devices were stressed using a HP4155 Semiconductor Parameter Analyzer with the bottom electrode grounded.

A schematic of the experimental setup used to carry out the IR mappings discussed in Section III is illustrated in Fig. 1. The core of the system is the Merlin-MID IR camera together with an external synchronization logic block implemented on a FPGA digital circuit. The IR camera presents a focal plane array (FPA) of 320×256 pixels InSb sensor (30×30 μm² pixel area) that guarantees a minimum temperature resolution of 25mK. The observation field is about 30 μm with a 1:1 optical magnification lens. The system is capable of detecting temperature distributions both in steady-state and transient conditions. In transient operation it is possible to use real-time and equivalent-time measurement modes. In the former case, the maximum sampling-rate is limited by the thermo-camera framerate to 50Hz. In the latter case, if the experiment can be repeated periodically, the system can reach an equivalent bandwidth of 100 kHz full-frame limited only by the minimum integration time of the FPA sensors (10μs). In this work, a direct method for transient characterization of the device temperature was used. The information provided by the system is subsequently edited using image processing software. More details about the IR mapping setup can be found in [12].

To conclude this Section, it is worth pointing out that the statistical study reported in Sections IV and V was carried out using the Spatstat package for the R language [13]. This package supports creation, manipulation and plotting of point patterns, exploratory data analysis, simulation of point process models, parametric model fitting, as well as many other statistical tools (including over 1500 user-level functions). Spatstat can be downloaded for free from the R website [14].

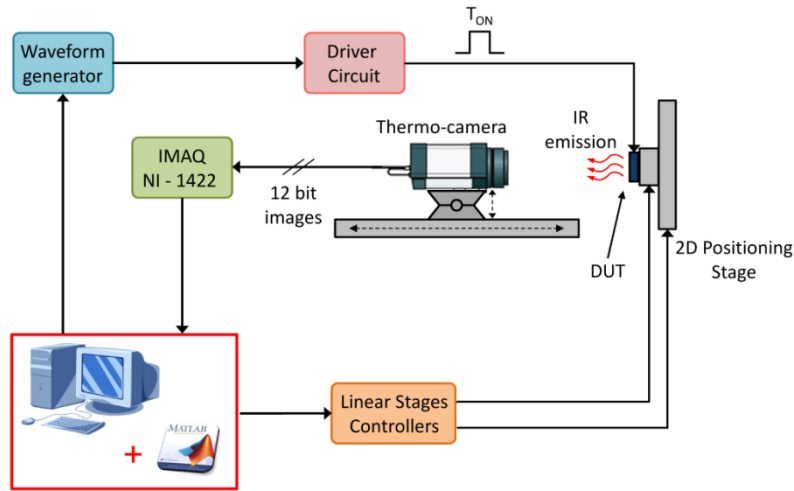


Fig. 1 Schematic of the experimental IR setup with detail of connections between different system parts.

3. GENERATION OF THE BD SPOTS AND THERMAL EFFECTS

The images shown in Fig. 2 illustrate the local temperature increase caused by the occurrence of a single and multiple BD events in the MIM devices described in Section II. The failure events were generated using CVS with stress voltages of about 8-9 V applied for periods not longer than 1 minute. In many cases the shorts between the top and bottom electrodes are permanent as revealed by the IR images. In other cases just a flash is observed, which indicates that after the metal evaporation, the electrical contact between the electrodes is locally lost. The voltage probe is clearly visible in the IR images too, which points out a temperature increase of the contact between the tip of the probe and the top electrode (see Fig. 2). A difference of up to eight degrees Celsius is detected between the metal electrode and the center of the leakage paths. Notice that this temperature can be radically different from the actual temperature reached inside the dielectric film during the micro-explosions. The IR images also show that the leakage current can be localized in a few sites (see Figs. 2.a and 2.b) or, if the damage is extremely severe, it can almost flow uniformly distributed over the whole device area (see Fig. 2.c). A thorough analysis of these experiments reveals that although the density of marks associated with the generation of BD spots on the top electrode can be quite large, the actual operating leakage current pathways spanning the dielectric film can be considerably less numerous. A second interesting question that arises is to what extent the local temperature increase associated with the formation of the current pathways does not affect the spatial generation of subsequent failure events. This issue will be analyzed in Sections IV and V in terms of the statistical distribution of the events. The results obtained by other authors using electrical methods indicate the absence of BD spot spatial correlation in MIS structures [15]. However, contrary to ours, that kind of study was limited to just a few BD events per device. In the next Section, the BD spot distribution in a 2-D space will be analyzed using a variety of functional estimators.

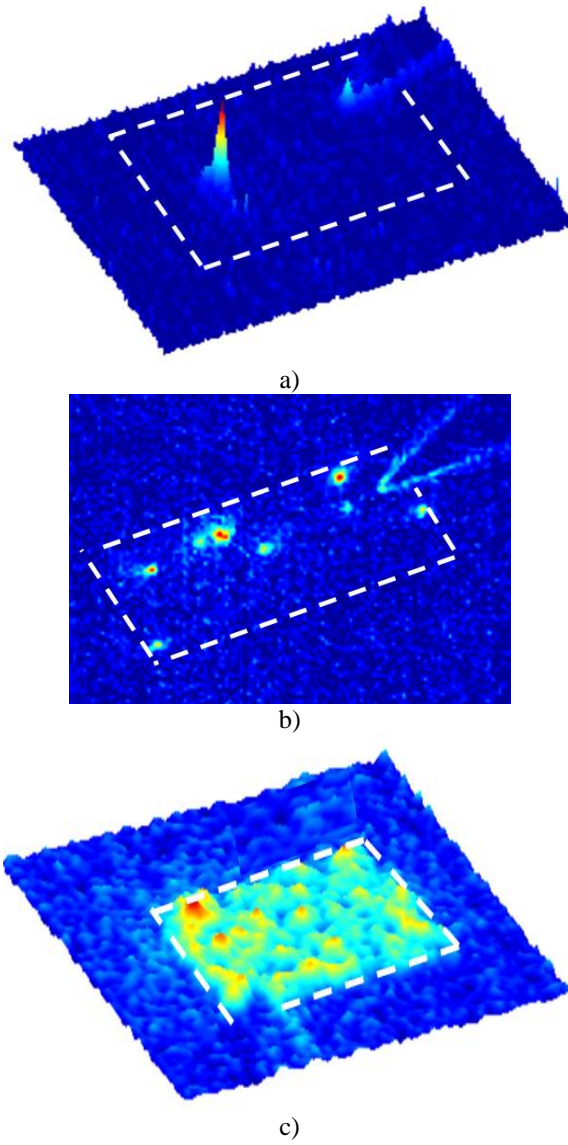


Fig. 2 Thermal images of different MIM structures in which a) single and b) and c) multiple BD spots are generated during electrical stress.

4. ANALYSIS OF THE BD SPOT DISTRIBUTION USING 2-D FUNCTIONAL ESTIMATORS

In order to characterize the BD spots distribution in a 2-D region, it is necessary first to provide a brief introduction to the different functional estimators that are considered in this study. Notice that the standard reference model of a point process in the plane is the

homogeneous Poisson point process, also referred to as *CSR* for Complete Spatial Randomness, which is commonly regarded as the null hypothesis model in spatial statistics [7]. The nearest neighbor distance distribution G is the cumulative distribution of the distance from a typical random point to the nearest other point (see Fig. 3). For a *CSR* process, G is given by the expression:

$$G_{CSR}(r) = 1 - \exp(-\lambda\pi r^2) \quad (1)$$

where λ is the average intensity of the process, i.e. the number of events registered divided by the area of the observation window. While $G > G_{CSR}$ suggests that nearest neighbor distances are shorter than for a *CSR* process (clustered pattern), $G < G_{CSR}$ suggests a regular pattern, or simply the absence of neighbor points. The empty space function F is the cumulative distribution of the distance from a fixed point in space (but arbitrary) to the nearest point. F is a useful statistic summarizing the sizes of gaps in the pattern. For a *CSR* process with intensity λ , F reads:

$$F_{CSR}(r) = 1 - \exp(-\lambda\pi r^2) \quad (2)$$

which coincides with the expression for the nearest neighbor distance distribution G_{CSR} . While $F > F_{CSR}$ suggests that empty space distances are shorter than for a *CSR* process (regularly space pattern), $F < F_{CSR}$ suggests a clustered pattern. The Ripley's K function is defined so that $\lambda K(r)$ equals the expected number of random points within a radius r of a typical random point. For a *CSR* process, K is given by the parabolic relationship:

$$K_{CSR}(r) = \pi r^2 \quad (3)$$

In this case, $K > K_{CSR}$ suggests clustering, while $K < K_{CSR}$ suggests a regular pattern. Perhaps the most important functional summary statistics available for point patterns is the pair correlation function g . This function expresses the probability of observing a pair of points separated by a distance r divided by the corresponding probability for a *CSR* process and can be found as:

$$g(r) = \frac{1}{2\pi r} \frac{dK(r)}{dr} \quad (4)$$

where $dK(r)/dr$ is the derivative of K with respect to r . In this case, $g > 1$ suggests clustering or attraction, while $g < 1$ suggests inhibition or regularity. For a *CSR* process $g_{CSR}(r)=1$. The estimator fails for r values close to 0 [7].

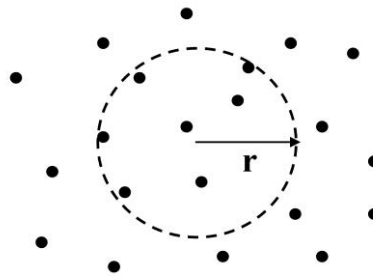


Fig. 3 Distribution of the points and circular region of generic radius r used to calculate the functional estimators.

In Figs. 4 to 6, three particular cases of MIM devices with BD spot patterns are shown. The images were obtained after the application of constant voltage stress. In the first two cases (Figs. 4 and 5), the voltage probe tip is clearly visible close to one corner of the device. The position of the probe tip defines the considered observation window (red solid line) within which the point pattern is analyzed. However, notice that for the analysis that follows, the specific location of the voltage probe is irrelevant, since r refers to a generic distance within the spatial point process. In the case of Fig. 4.a, the area of the device is $400 \times 400 \mu\text{m}^2$, the area of the observation window is $370 \times 370 \mu\text{m}^2$ and the number of spots registered is 321. This corresponds to a density of 2.35×10^{-3} points/ μm^2 . The dashed lines in Figs. 4.b to 4.e were calculated using expressions (1)-(4) for a *CSR* process. Notice that the estimated curves (black solid lines) are all confined within the 95% confidence bands (shaded area) except for some deviation detected in G for the short distance range. This is merely a consequence of considering the BD spots as mathematical points (recall that typical lateral sizes are about 2 to 3 μm) [16]. In addition, notice that g fluctuates around the unity mark, which is indicative of a *CSR* process at different scales. In summary, the process illustrated in Fig. 4 can be considered a *CSR* process. No interaction is detected among the BD spots, i.e. they are spatially uncorrelated. Something similar occurs for the device shown in Fig. 5.a. In this case the area of the device is $400 \times 100 \mu\text{m}^2$, the area of the observation window is $392.5 \times 94.5 \mu\text{m}^2$ and the number of spots is 168. This corresponds to a density of 4.53×10^{-3} points/ μm^2 , which almost doubles the intensity of the previous example. No interpoint distance below 2 μm is registered but this is again a matter related to the spot sizes. No sign of deviation from a *CSR* process is detected. The case illustrated in Fig. 6.a is rather different since one of the sides of the device is significantly larger than the other. The device under consideration has lateral sizes of $1600 \times 100 \mu\text{m}^2$ and the region of interest (observation window) coincides with the device area. In this case, 132 points were registered with an average density of 8.25×10^{-4} points/ μm^2 . Notice the important deviations that take place with respect to the corresponding *CSR* process (see for example the pair correlation function g in Fig. 6.e). Particularly important is the absence of points in the short distance range ($<5 \mu\text{m}$), but this can be related to the low density of points ($\sim 10^{-4}$) investigated. For the example illustrated in Fig. 6.a, the information about the location of the voltage probe is unavailable. The estimators seem to indicate that the data points follow a *CSR* process for distances larger than 5-10 μm . The deviation in G for the long distance range ($>30 \mu\text{m}$) can be attributed to edge effects associated with the low aspect ratio (100/1600) of the investigated device (see Fig. 6.b). In Section V, the same BD spot patterns explored in this Section are assessed again but in connection with the probe point location. Since no spatial correlation effects were detected using 2-D functional estimators, it is expected these results to be confirmed using alternative methods such as the point-to-event distance and angular probability distributions. This analysis is accomplished in the next Section.

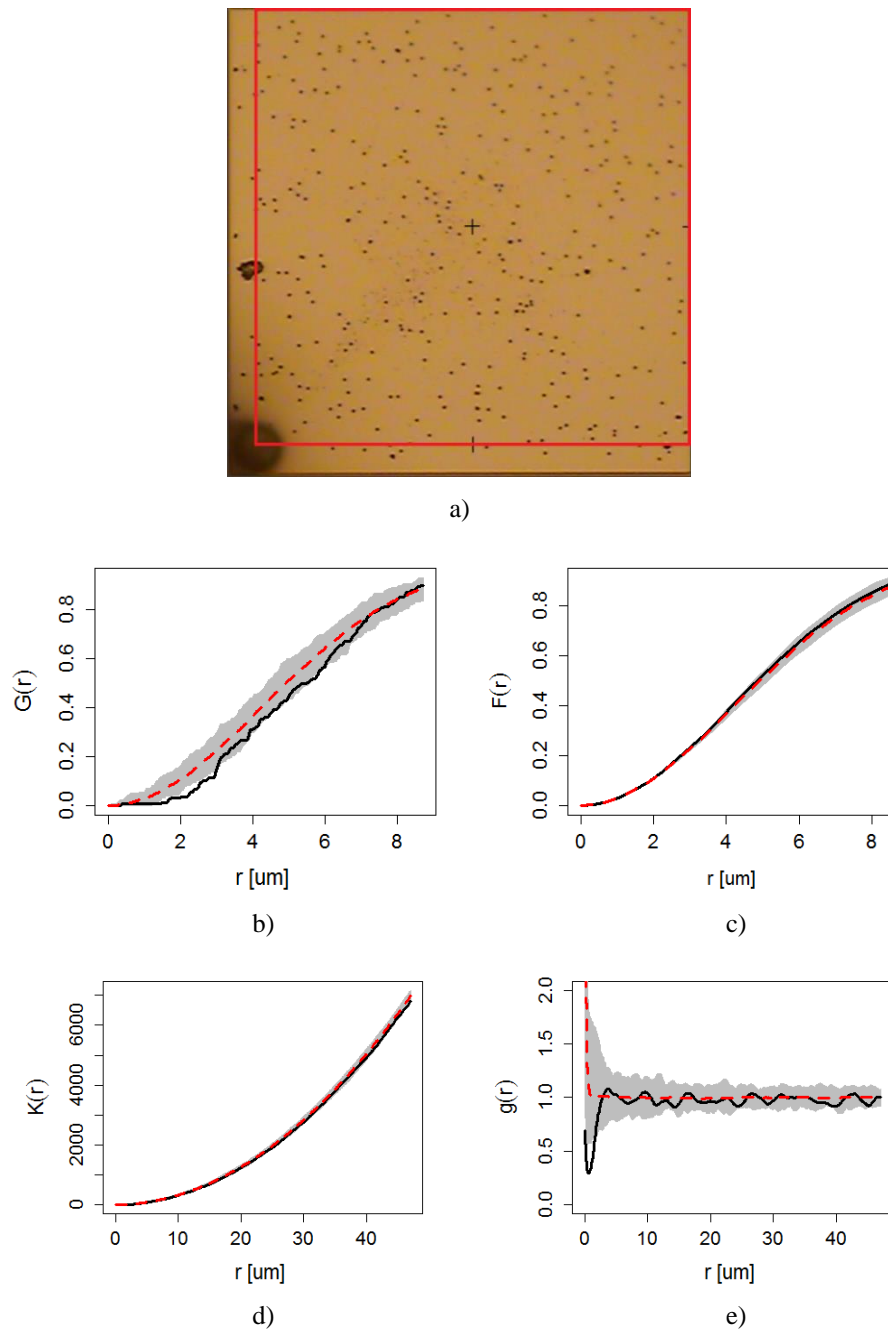
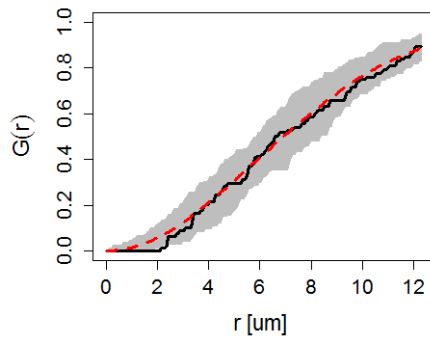


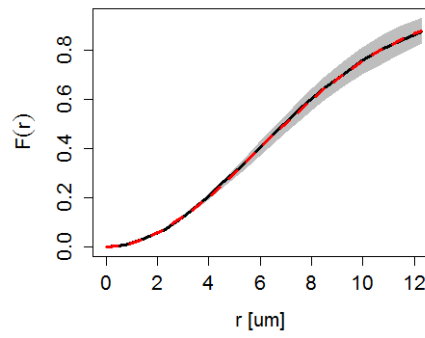
Fig. 4 a) Distribution of the BD spots in a MIM device with area $400 \times 400 \mu\text{m}^2$. 2-D functional estimators: b) G , c) F , d) K and e) g .



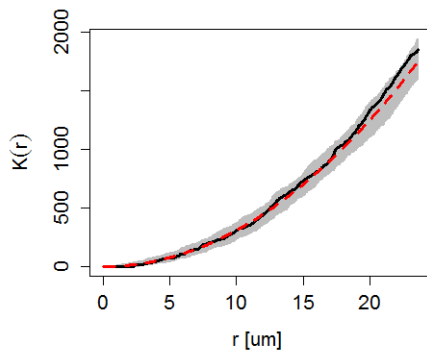
a)



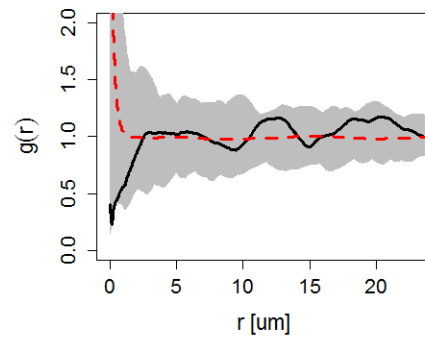
b)



c)



d)

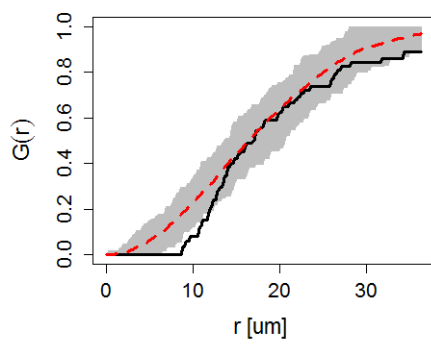


d)

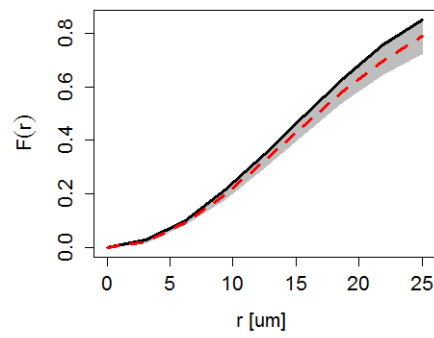
Fig. 5 a) Distribution of the BD spots in a MIM device with area $400 \times 100 \mu\text{m}^2$. 2-D functional estimators: b) G , c) F , d) K and e) g .



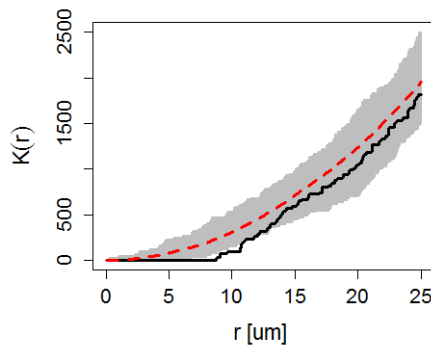
a)



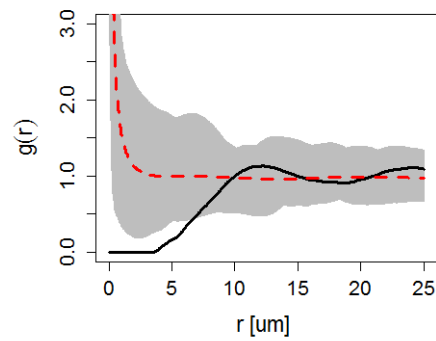
b)



c)



c)



d)

Fig. 6 a) Distribution of the BD spots in a MIM device with area $1600 \times 100 \mu\text{m}^2$.
2-D functional estimators: b) G , c) F , d) K and e) g .

5. ANALYSIS OF THE BD SPOT DISTRIBUTION USING POINT-TO-EVENT DISTRIBUTIONS

In order to perform the study on the spatial distribution of the BD spots with respect to a particular point in the plane, it is necessary to characterize the locations of the failure events by two random variables (see Fig. 7): i) the distance $0 \leq x \leq (a^2 + b^2)^{1/2}$ between the reference point P and the event E and, ii) the angle $0 \leq \alpha \leq \pi/2$ subtended by the line connecting P with E measured with respect to the horizontal side of the rectangle $a \times b$. In particular, for our analysis, we take P as the location of the voltage probe, which is chosen to coincide with one vertex of the observation window. This selection remarkably simplifies the mathematical treatment. The variable x defines the point-to-event distance probability distribution function (PDF) $f(x)$, whereas α defines the point-to-event angular probability distribution function $f(\alpha)$. $F(x)$ and $F(\alpha)$ denote the corresponding cumulative distribution functions (CDF). For the sake of simplicity, we use the same notation f and F for both variables though their explicit mathematical expressions are different. These distributions can be easily found by combining the areas of geometrical figures (see Ref.[17]).

The PDF and CDF for the distance x are given by the expressions:

$$f(x) = \begin{cases} \frac{\pi x}{2ab} & 0 \leq x < a \\ \frac{x}{ab} \arcsin\left(\frac{a}{x}\right) & a \leq x < b \\ \frac{x}{ab} \left[\arcsin\left(\frac{a}{x}\right) - \arccos\left(\frac{b}{x}\right) \right] & b \leq x \leq \sqrt{a^2 + b^2} \end{cases} \quad (5)$$

and

$$F(x) = \begin{cases} \frac{\pi x^2}{4ab} & 0 \leq x < a \\ \frac{1}{2ab} \left[ax \sqrt{1 - \frac{a^2}{x^2}} + x^2 \arcsin\left(\frac{a}{x}\right) \right] & a \leq x < b \\ \frac{1}{2ab} \left[ax \sqrt{1 - \frac{a^2}{x^2}} + x^2 \arcsin\left(\frac{a}{x}\right) + bx \sqrt{1 - \frac{b^2}{x^2}} - x^2 \arccos\left(\frac{b}{x}\right) \right] & b \leq x \leq \sqrt{a^2 + b^2} \end{cases} \quad (6)$$

respectively. The PDF and CDF for the angle α are given by the expressions:

$$f(\alpha) = \begin{cases} \frac{b}{2a} \frac{1}{\cos^2(\alpha)} & 0 < \alpha < \arctan\left(\frac{a}{b}\right) \\ \frac{a}{2b} \frac{1}{\sin^2(\alpha)} & \arctan\left(\frac{a}{b}\right) \leq \alpha \leq \frac{\pi}{2} \end{cases} \quad (7)$$

and

$$F(\alpha) = \begin{cases} \frac{b}{2a} \tan(\alpha) & 0 < \alpha < \arctan\left(\frac{a}{b}\right) \\ 1 - \frac{a}{2b} \tan\left(\frac{\pi}{2} - \alpha\right) & \arctan\left(\frac{a}{b}\right) \leq \alpha \leq \frac{\pi}{2} \end{cases} \quad (8)$$

respectively.

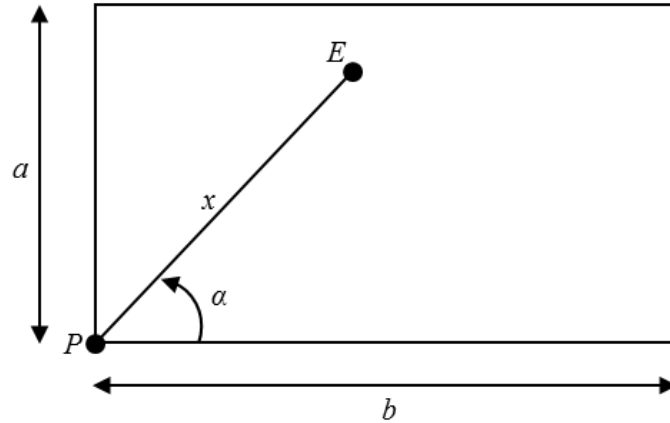


Fig. 7 Definition of the variables used to localize the breakdown spots (E) with respect to the voltage probe position (P). x is the distance from P to E and α is the corresponding angle.

Figures 8 to 10 show the three cases discussed in the previous Section but now emphasizing the distribution of the points with respect to the bottom-left vertex of the observation window. As expected, the experimental results (histograms for the PDFs and black solid lines for the CDFs) agree well with the theoretical results (red solid lines) calculated using expressions (5)-(8). Notice how the mode of the distributions shifts to the left (shorter distances and smaller angles) as the length of the rectangle increases. In all the analyzed cases, it can be concluded that the data points are *CSR* distributed in total consistency with the observations reported in Section IV. Notice that a fundamental difference between the method presented here and that of the functional estimators is that the former one makes explicit reference to the shape of the observation while the second does not (no edge correction has been considered). On the other hand, methods for calculating the confidence bands are ready available for the functional estimators, whereas these methods for the point-to-event distributions have not been developed yet.

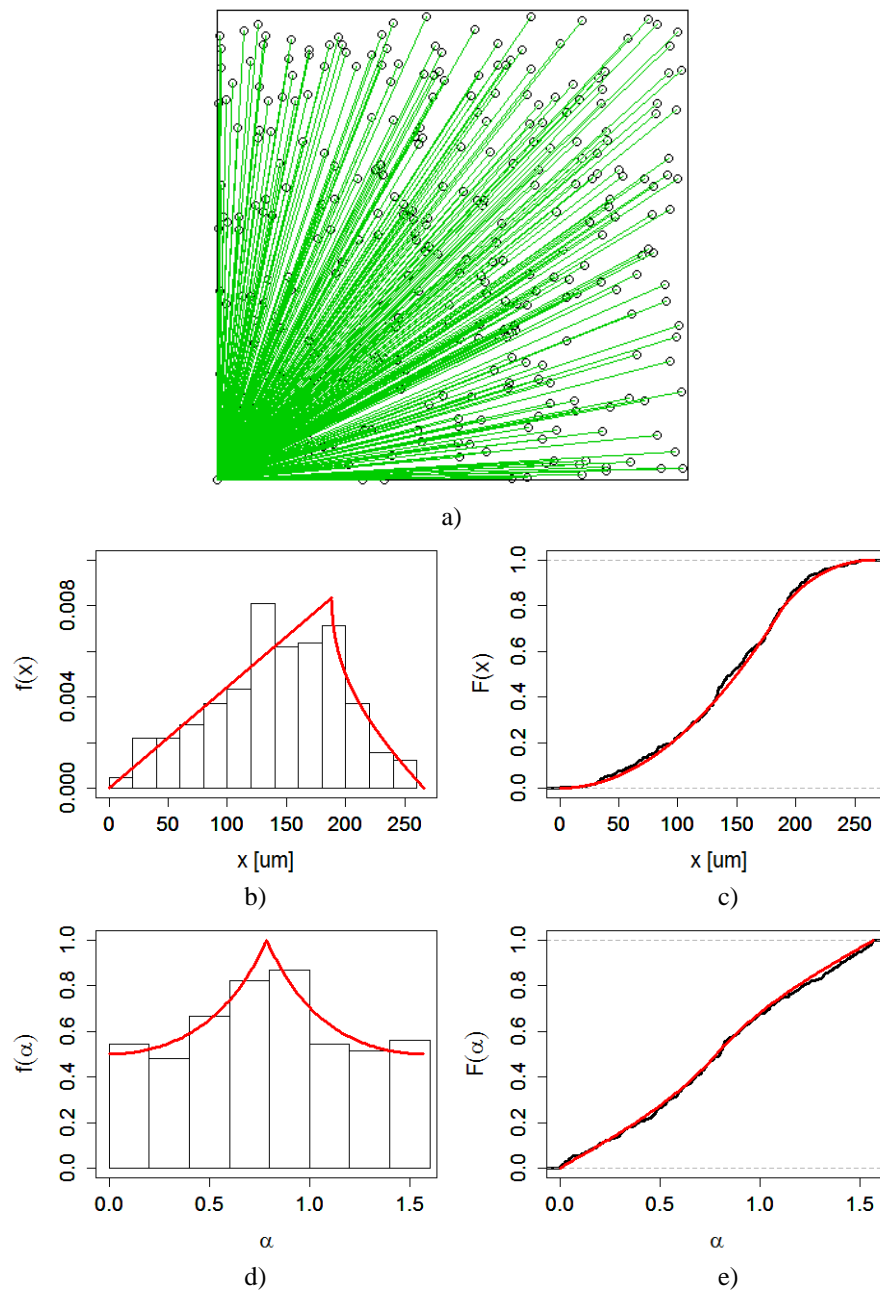


Fig. 8 a) Map of the BD spots in a MIM device with area $400 \times 100 \mu\text{m}^2$. The lines indicate the distances from the event to the bottom-left vertex of the observation window. PDFs and CDFs for the distances x and the angles α : b) $f(x)$, c) $F(x)$, d) $f(\alpha)$ and e) $F(\alpha)$.

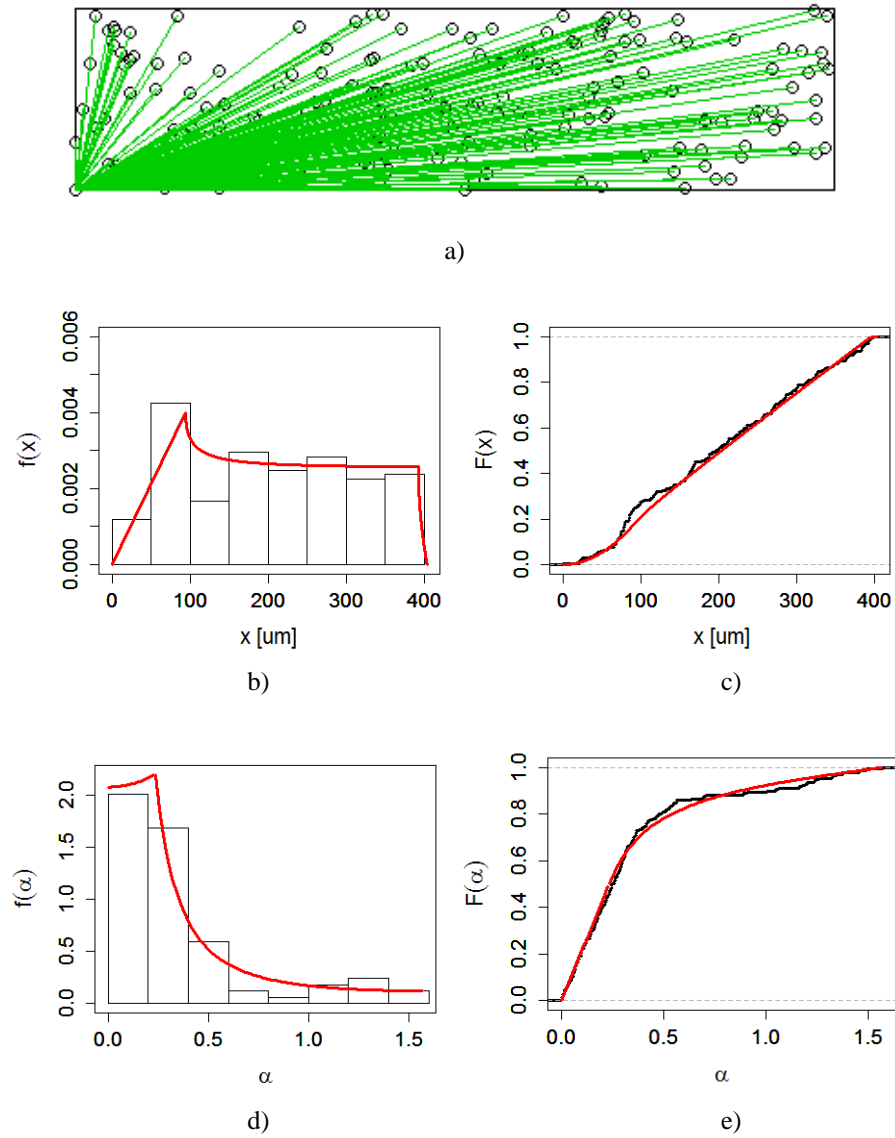


Fig. 9 a) Map of the BD spots in a MIM device with area $400 \times 100 \mu\text{m}^2$. The lines indicate the distances from the event to the bottom-left vertex of the observation window. PDFs and CDFs for the distances x and the angles α : b) $f(x)$, c) $F(x)$, d) $f(\alpha)$ and e) $F(\alpha)$.

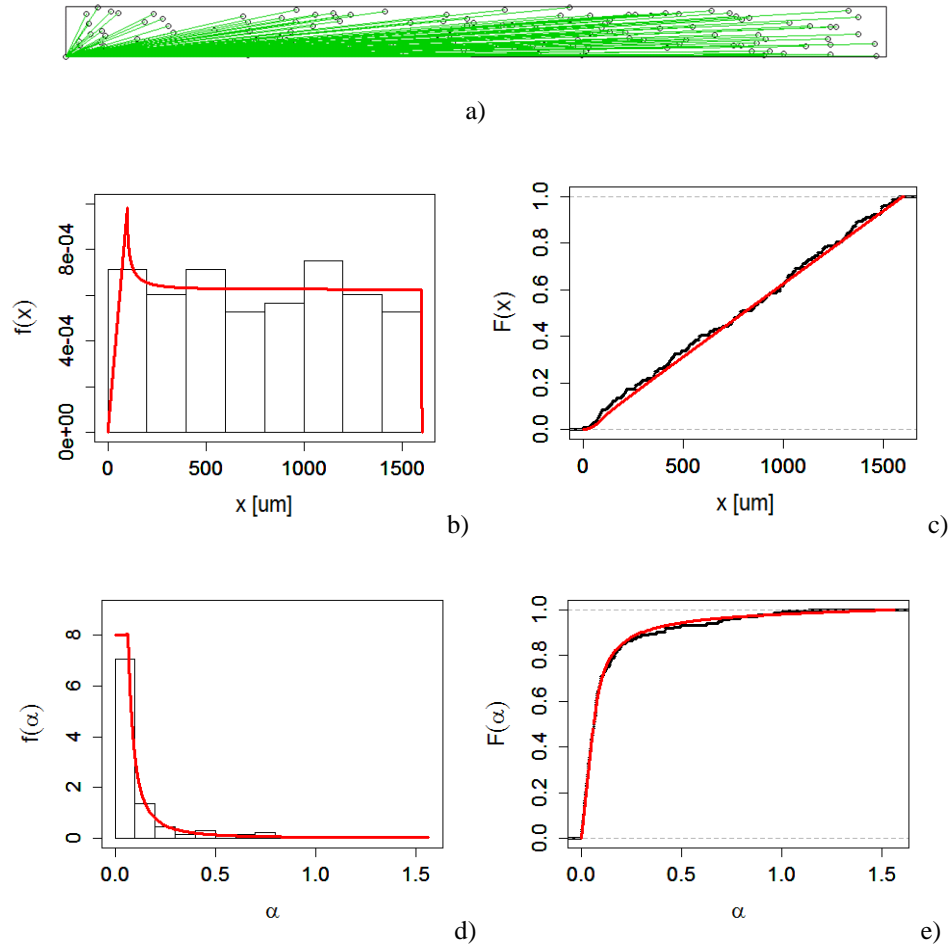


Fig. 10 a) Map of the BD spots in a MIM device with area $1600 \times 100 \mu\text{m}^2$. The lines indicate the distances from the event to the bottom-left vertex of the observation window. PDFs and CDFs for the distances x and the angles α : b) $f(x)$, c) $F(x)$, d) $f(\alpha)$ and e) $F(\alpha)$.

6. CONCLUSIONS

The spatial distribution of breakdown spots in HfO₂-based large area MIM capacitors generated by severe electrical stress was investigated. The analysis was performed on devices with different aspect ratios. Using real-time IR mapping it was demonstrated that the occurrence of these shorts between the top and bottom metal electrodes is associated with a notable local temperature increase. However, not all the generated spots remain conducting after their creation because of the volatilization of the top metal electrode. From the statistical analysis carried out in this work, it can be concluded that the breakdown spots in MIM devices with high-*K* dielectric are spatially uncorrelated. This is consistent with previous observations carried out on MIS devices.

Acknowledgement: *This work is funded in part by the Spanish Ministry of Science and Technology under contract TEC2012-32305 and the DURSI of the Generalitat de Catalunya under contract 2009SGR783.E. Miranda thanks the funding from the Visiting Professor Program of the University of Naples Federico II. The authors also acknowledge I. M Povey, E. O'Connor, K. Cherkaoui and P.K. Hurley (Tyndall National Institute, Cork, Ireland) for device provision and assistance in the electrical characterization of the samples. We give our special thanks to Prof. Ninoslav Stojadinović and Prof. Danijel Danković from University of Niš, Republic of Serbia for their invitation to write this report..*

REFERENCES

- [1] A. Oates, "Reliability issues for high-*K* gate dielectrics", *IEDM Tech. Dig.*, 2003, pp. 923-926.
- [2] E. Wu, J. Stathis, and L. Han, "Ultra-thin oxide reliability for ULSI applications", *Semicond. Sci. Technol.* 15, 425 (2000).
- [3] M. Alam, R. Smith, B. Weir, and P. Silverman, "Thin dielectric films: Uncorrelated breakdown of silicon integrated circuits", *Nature* 420, 378 (2002).
- [4] J. Suñé and E. Wu, "Statistics of successive breakdown events in gate oxides", *IEEE Elect. Dev. Lett.* 24, 272 (2003)
- [5] X. Saura, D. Moix, J. Suñé, P.K. Hurley, and E. Miranda, "Direct observation of the generation of breakdown spots in MIM structures under constant voltage stress", *Mic. Rel.* 53, 1257 (2013).
- [6] E. Miranda and J. Suñé, "Electron transport through broken down ultra-thin SiO₂ layers in MOS devices", *Mic. Rel.* 44, 1 (2004).
- [7] J. Illian, A. Penttinen, H. Soyan, and D. Stoyan, in *Statistical analysis and modelling of spatial point patterns*, Wiley, 2008.
- [8] P. Diggle, in *Statistical analysis of spatial point patterns*, Arnold, 2003.
- [9] R. Waser, R. Dittmann, G. Stakov, and K. Szot, "Redox-based resistive switching memories - nanoionic mechanisms, prospects, and challenges", *Adv. Mat.* 21, 2632 (2009).
- [10] R. Waser and M. Aono, "Nanoionics-based resistive switching memories", *Nature Materials* 6, 833 (2007).
- [11] S. Lombardo, J. Stathis, B. Linder, Kin Leon Pey, F. Palumbo, and Chih Hang Tung, "Dielectric breakdown mechanisms in gate oxides", *J. Appl. Phys.* 98, 121301 (2005).
- [12] M. Riccio, G. Breglio, A. Irace, and P. Spirito, "An equivalent time temperature mapping system with a 320 x 256 pixels full-frame 100 kHz sampling rate", *Rev. Sci. Instrum.* 78, 106106 (2007).
- [13] A. Baddeley, R. Turner, "Spatstat: An R Package for Analyzing Spatial Point Patterns", *J. Stat. Software* 12, 1 (2005).
- [14] www.r-project.org
- [15] M. Alam, D. Varghese, and B. Kaczer, "Theory of breakdown position determination by voltage- and current-ratio methods", *IEEE Trans. Elect. Dev.* 55, 3150 (2008).
- [16] X. Saura, J. Suñé, S. Monaghan, P.K. Hurley, and E. Miranda, "Analysis of the breakdown spot spatial distribution in Pt/HfO₂/Pt capacitors using nearest neighbor statistics", *J. Appl. Phys.* 114, 154112 (2013).
- [17] S. Chiu and R. Larson, "Bertrand's paradox revisited: More lessons about that ambiguous word: Random", *J. Ind. Sys. Eng.* 3, 1 (2009).